International Journal of
Turbomachinery
Propulsion and Power

MDPI

Article

Reynolds Sensitivity of the Wake Passing Effect on a LPT Cascade Using Spectral/*hp* Element Methods†

Andrea Cassinelli [1], Andrés Mateo Gabín [2], Francesco Montomoli [1], Paolo Adami [3], Raul Vázquez Díaz [4] and Spencer J. Sherwin [1,*]

[1] Department of Aeronautics, Imperial College London, London SW7 2AZ, UK; andrea.cassinelli.93@gmail.com (A.C.); f.montomoli@imperial.ac.uk (F.M.)
[2] School of Aeronautical and Space Engineering, Universidad Politécnica de Madrid, 28040 Madrid, Spain; andres.mgabin@upm.es
[3] Rolls-Royce Deutschland, 15827 Dahlewitz, Germany; Paolo.Adami2@Rolls-Royce.com
[4] Rolls-Royce plc., Derby DE24 8ZF, UK; Raul.Vazquez@Rolls-Royce.com
* Correspondence: s.sherwin@imperial.ac.uk
† This paper is an extended version of our paper published in Proceedings of the European Turbomachinery Conference ETC14 2021, Paper No. 606.

Abstract: Reynolds-Averaged Navier–Stokes (RANS) methods continue to be the backbone of CFD-based design; however, the recent development of high-order unstructured solvers and meshing algorithms, combined with the lowering cost of HPC infrastructures, has the potential to allow for the introduction of high-fidelity simulations in the design loop, taking the role of a virtual wind tunnel. Extensive validation and verification is required over a broad design space. This is challenging for a number of reasons, including the range of operating conditions, the complexity of industrial geometries and their relative motion. A representative industrial low pressure turbine (LPT) cascade subject to wake passing interactions is analysed, adopting the incompressible Navier–Stokes solver implemented in the spectral/*hp* element framework *Nektar*++. The bar passing effect is modelled by leveraging a spectral-element/Fourier Smoothed Profile Method. The Reynolds sensitivity is analysed, focusing in detail on the dynamics of the separation bubble on the suction surface as well as the mean flow properties, wake profiles and loss estimations. The main findings are compared with experimental data, showing agreement in the prediction of wake traverses and losses across the entire range of flow regimes, the latter within 5% of the experimental measurements.

Keywords: wake-passing effect; reynolds sensitivity; spectral/*hp* element method; high-order; smoothed profile method

check for updates

Citation: Cassinelli, A.; Mateo Gabín, A.; Montomoli, F.; Adami, P.; Vázquez Díaz, R.; Sherwin, S.J. Reynolds Sensitivity of the Wake Passing Effect on a LPT Cascade Using Spectral/*hp* Element Methods. *Int. J. Turbomach. Propuls. Power* **2022**, *1*, 0. https://doi.org/

Academic Editor: Marcello Manna, Tony Arts

Received: 20 June 2021
Accepted: 7 February 2022
Published:

Publisher's Note: MDPI stays neutral with regard to jurisdictional claims in published maps and institutional affiliations.

Copyright: © 2022 by the authors. Licensee MDPI, Basel, Switzerland. This article is an open access article distributed under the terms and conditions of the Creative Commons Attribution (CC BY-NC-ND) license (https://creativecommons.org/licenses/by-nc-nd/4.0/).

1. Introduction

In a gas turbine engine, the pressure expansion through high- and low-pressure turbines (LPT) is achieved in a number of subsequent stages. The interaction of multiple stages of rotors and stators is a crucial source of deterministic unsteadiness, which has effects on the loss production mechanisms, and it is thus of great importance to designers. One of the early computational investigations of the wake-passing effect was carried out by Wu and Durbin [1,2], who presented evidence that incoming wakes are responsible for the formation of longitudinal structures on the pressure side.

Subsequently, a number of Direct Numerical Simulation (DNS) studies were performed on LPTs, providing further contributions to the understanding of the effect of incoming wakes on the pressure- and suction-side boundary layers [3–6]. A detailed review by Hodson and Howell [7] summarises the wake-induced boundary layer transition mechanisms in LPTs.

The impact of the wake passing frequency on loss mechanisms has been numerically investigated by several authors. Michelassi et al. [8] built on top of previous work [9] to analyse the effects of various types of inflow disturbances on losses in a series of compressible DNS simulations. In particular, they observed the effect of three reduced frequencies and two Reynolds numbers ($Re_2 = 60{,}000$ and 100,000) on various types of loss indicators. The behaviour of high reduced frequencies was found to be most effective in suppressing the suction surface separation bubble, by manifesting a very similar behaviour to high levels of inflow turbulence, due to the constant-area mixing prior to the leading edge.

The comparisons of mixed-out losses with profile losses as defined by Denton [10] allowed distinguishing the losses generated in the boundary layer from those generated in the flow core by the variable-area wake mixing. The largest difference was found at low levels of reduced frequency (1 bar per pitch): in this case, the wakes remain distinct within the blade passage and experience significant wake distortion losses.

Further LES simulations [11] demonstrated the combined importance of the reduced frequency and flow coefficient on losses. These important design parameters affect the frequency with which incoming wakes impact on the cascade as well as the wake inclination. The normal distance between incoming wakes was found to correlate very well with mixed-out losses, further confirming that wake merging (which produces a free-stream turbulence-like behaviour) is generally beneficial for the reduction of unsteady losses. This approach can importantly be adopted to inform design optimisation, as the various combinations of reduced frequency and flow coefficient are effectively a consequence of design parameters, such as the revolution speed and flow-through velocity.

As part of an ongoing effort to develop a validated incompressible DNS capability for the turbomachinery Industry using spectral/*hp* element methods, the present work builds on consolidated expertise [12,13] in the use of the *Nektar*++ open-source software framework [14] for industrial applications. The wake-passing effect is analysed in the context of a representative research LPT profile, witha particular focus on the Reynolds sensitivity of the transition mechanism on the suction surface and the loss prediction. The optimal and most realistic degree of reaction corresponds to the reduced frequency range where unsteady losses are highest [11], which is targeted in this paper. The availability of experimental data in the wake traverses at the flow regimes analysed allows quantification of the accuracy of the numerical approach.

The paper is organised as follows: first, a brief introduction on the numerical setup and wake modelling strategy is presented. Subsequently, the flow dynamics on the suction surface are characterised in the various phases of the wake passing cycle. The following sections focuses on the time-averaged effects of the wake passing, analysing the blade wall distributions, wake profiles and mixed-out measurements and establishing a comparison with highly accurate experimental data. The paper concludes by providing remarks on the validity of the results presented.

2. Methods

2.1. Numerical Approach

The incompressible Navier–Stokes equations

$$\frac{\partial \mathbf{u}}{\partial t} = -(\mathbf{u}\cdot\nabla)\mathbf{u} - \nabla p + \nu\nabla^2\mathbf{u} \qquad \text{in}\,\Omega\,, \tag{1}$$

$$\nabla\cdot\mathbf{u} = 0 \qquad \text{in}\,\Omega\,, \tag{2}$$

were discretised using the spectral/*hp* element framework *Nektar*++ [14]. The solver adopts a stiffly stable time discretisation [15], which decouples the velocity and pressure fields, also known as the Velocity-Correction Scheme [16]. This formulation treats the convective terms explicitly, while pressure and the viscous contributions are treated implicitly; therefore, addressing stability constraints that would otherwise be associated with the viscous time stepping.

Analysis of test cases at high Reynolds numbers with under-resolved meshes requires the use of stabilization techniques: if the dissipative scales at high wavenumbers are not fully resolved, a buildup of energy might cause the solution to diverge. Spectral Vanishing Viscosity (SVV) was introduced by Tadmor et al. [17] as a technique to add artificial diffusion to potentially unstable under-resolved scales. Since the oscillations causing divergence of the solution emerge at sub-elemental level, SVV is a stabilization technique that acts at the subgrid-scale level, without introducing any explicit model.

The DG-Kernel SVV formulation introduced by Moura et al. [18,19] was adopted to ensure numerical stability in the spectral/*hp* planes, while the traditional exponential kernel was employed in the Fourier expansion in the spanwise direction. In adopting such a stabilisation approach, better resolution ability is achieved by increasing the polynomial order (both in terms of diffusion and dispersion properties) as opposed to reducing the base mesh size. As shown in the earlier work of Cassinelli et al. [12] at $Re = 88{,}000$, the polynomial order adopted is sufficiently high for SVV not to affect the flow physics of interest. The spectral/*hp* dealiasing approach by [20] was adopted for all computations. The spectral/*hp* element implementation of the present work relies on Taylor–Hood type elements, where the C^0 continuous pressure field is computed at one polynomial order lower than the C^0 continuous velocity variables. Further details on the numerical methodology, mesh resolution and convergence properties were discussed by Cassinelli et al. [12,21].

2.2. LPT Setup with Wake Passing

The availability of experimental data motivated the choice of the flow regimes in analysis. Three Reynolds numbers were considered: $Re_2 = 86{,}000, 157{,}000$, and $297{,}000$, based on mixed-out exit velocity U_2 and suction surface perimeter S_0. The research LPT cascade in analysis is scaled by the true chord and inflow velocity, so that $C = 1$ and $U_\infty = 1$.

The wake-passing effect is experimentally reproduced by including a mechanism to introduce upstream-generated wakes shed from uniformly spaced cylindrical bars, controlled by an electric motor. To analyse this phenomenon, two nondimensional parameters are of fundamental importance: the reduced frequency F_{red} and flow coefficient Φ, defined as:

$$F_{\text{red}} = \frac{U_b C}{P_b U_2}, \qquad \Phi = \frac{U_{\infty,x}}{U_b}, \tag{3}$$

where U_b indicates the bar velocity, P_b is the vertical distance between bars and $U_{\infty,x}$ is the axial inlet velocity. These parameters control the bar speed (which affects the inclination of the wake when it impinges on the blade) and their relative distance. Together, they affect the frequency at which the wakes impact on the blade. Adjusting the cylinder distance and speed allows for analysis of realistic configurations where the rotor and stator count are different. However, the numerical experiments are typically carried out with pitchwise periodic boundary conditions.

Limitations owing to the computational cost that would be required to simulate multiple blades require the cascade pitch P_y to be a multiple of the distance between bars P_b. Therefore, from a computational perspective, the control parameter in the simulations is the velocity of the cylinders. In this study, the exact value of the reduced frequency was simulated, while the flow parameter was enforced as a consequence of single-pitch periodicity (i.e., imposing $P_b = P_y$). The numerical values imposed in the simulations are reported in Table 1. The relative error between the nominal flow coefficient and effective flow coefficient is 6.748%. The lower flow coefficient results in slightly higher wake inclination compared to the experiments.

Introducing the wake passing period $\mathcal{T}_b = P_b/U_b$, time can be expressed as function of the number of periods m and the phase $0 \leq \varphi \leq 1$: $t = m\mathcal{T}_b + \varphi\mathcal{T}_b$. After transient times of at least $12C/U_\infty$, time-averaged statistics were subsequently sampled over $m = 20$ bar passing periods (under $T = 24C/U_\infty$). At phase $\varphi = 0$, the bar is situated at the same pitchwise location as the leading edge, $y/C = 0$.

Table 1. LPT bar passing setup with cylinder parameters in the upper portion of the table. Re_2 = 86,000 was simulated both with inflow wakes (IW) and inflow turbulence (IT), while other regimes analyse IW alone. The compute time is estimated on 1000 cores on the Archer supercomputer, including runtime post-processing and thus providing a conservative estimate.

Re_2	86,000 (IW, IW+IT)	157,000 (IW)	297,000 (IW)
F_{red} (S_0-based)	0.624132	0.627675	0.633188
$U_b^{\text{sim}}/U_\infty$	0.705339	0.706414	0.708116
Φ^{sim}	1.17731	1.17414	1.16966
α_1 [°]	33.86	33.96	34.08
Δt	2.5×10^{-5}	2.5×10^{-5}	2×10^{-5}
Compute time for $T = 1C/U_\infty$	8 h 40 min	8 h 40 min	10 h 45 min

The x–y planes were discretised with a high-order expansion at $P = 6$; the spanwise domain was set to $L_z = P_y/4 = 0.21164\,C$ and discretised with $N_z = 72$ Fourier planes, resulting in 52.67 M DoF per variable. As shown in Figure 1, this numerical setup yields a wall resolution of $\Delta x^+ < 20$, $\Delta y^+ < 0.6$, $\Delta z^+ < 8$ at $Re_2 = 297{,}000$. The space- and time-convergence properties of a similar numerical setup on a range of statistical distributions and properties were previously assessed extensively in a clean inflow case at $Re = 88{,}000$ [12]. In particular, $x - y$ plane convergence was analysed by means of P-refinement, reporting negligible discrepancies for expansion orders $P > 5$. The independence of the results with respect to the span was also discussed, and further evaluated by analysis of the correlation function [21], which showed that the blade wake is fully contained within the chosen spanwise domain. It should be noted that the aforementioned analyses were carried out in a previous study in the context of a disturbance-free inflow environment, at a flow regime corresponding to the lower end of the Reynolds envelope considered in the present study. Furthermore, since the same mesh is employed for all Reynolds numbers, the effective resolution is lower at high Reynolds numbers.

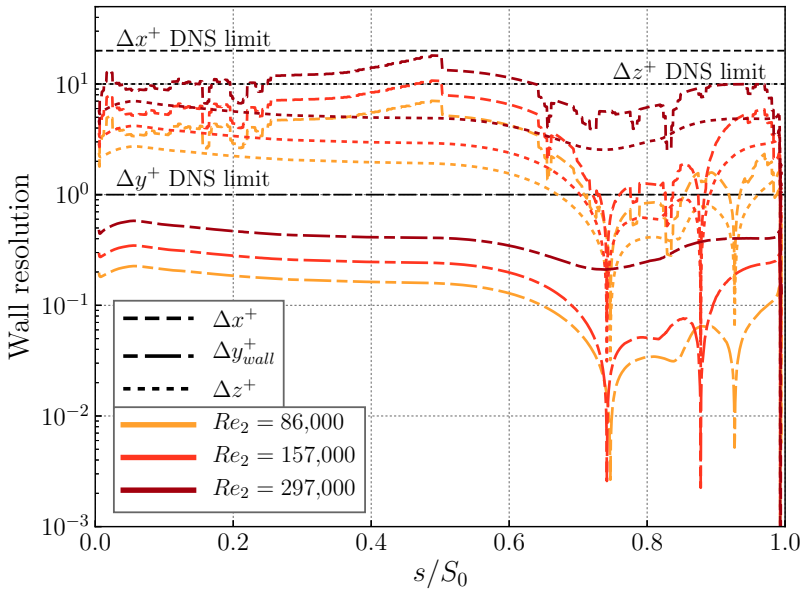


Figure 1. Wall resolution along the suction surface with increasing Re_2 and incoming wakes.

Enforcing the pitchwise domain to be a multiple of the spanwise domain allowed adopting a modified version of the inflow turbulence generation algorithm by Davidson [22], introduced and validated in *Nektar++* [13]. This implementation allows to generate a

spanwise- and pitchwise-periodic synthetic velocity signal, requiring a choice of spanwise domain such that P_y is a multiple of L_z.

Case $Re_2 = 86{,}000$ is analysed with and without inflow turbulence (on top of the discrete disturbances shed by passing bars). The inflow turbulence case (IW+IT) required a refined computational mesh to resolve the turbulent structures introduced at the inlet. This mesh differs from the IW mesh only in the region comprised between the inflow and the vertically refined line where the bar passing occurs. A nominal inflow turbulence intensity TI $= 3.5\%$ was prescribed in combination with a length scale $L_t = 0.05C$ to guarantee domain independence.

The algorithm selected 30 modes to discretise the modified von Kármán spectrum, compared to 1024 specified previously analysed [13]. As a consequence of a coarser discretisation of the wavenumber space, the level of turbulence intensity effectively introduced at the inlet of the computational domain is lower than prescribed: TI $= 2.578\%$.

2.3. Modelling the Bar Passing Effect

To model the bar passing effect, the Smoothed Profile Method (SPM), first introduced by Nakayama and Yamamoto [23], was selected. The method was further developed to adopt a time discretisation based on a high-order semi-implicit splitting scheme [24,25], and incorporated in the *Nektar++* framework. Extensive preliminary validation was carried out in the PhD thesis by Cassinelli [21] to ensure the generation of a realistic cylinder wake.

As part of the SPM formulation, an interface thickness parameter must be selected to represent the rigid particles. The interface thickness was selected to ensure accurate representation of the SPM boundaries (thus driven by resolution requirements). An auxiliary study focused on varying the diameter of the cylinders at fixed interface thickness. A smaller bar diameter of $d_b^{\mathrm{SPM}} = 0.6d_b$ (with $d_b/C = 0.023$) produced wake profiles and spectral characteristics matching those of a corresponding DNS simulation over the entire range of Reynolds numbers analysed.

The qualitative result of the wake-passing effect at high Reynolds number is shown in Figure 2. The initial stage of wake bending is visible in the Figure, while the suction surface transition leads to fully turbulent boundary layer at the trailing edge.

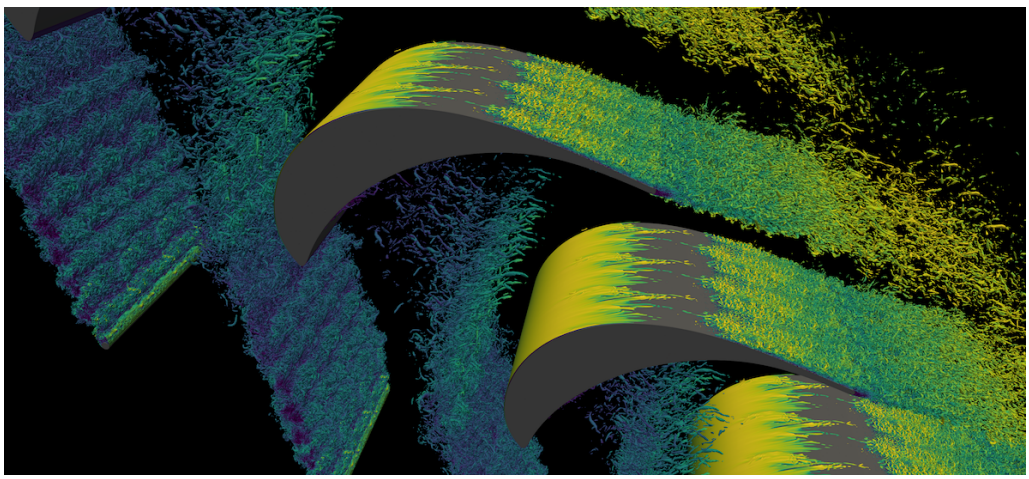


Figure 2. Iso-surfaces of Q-Criterion ($Q = 200$) contoured by velocity magnitude in case $Re_2 = 297{,}000$. The computational domain is duplicated for graphical purposes.

2.4. Low-Speed Experimental Testing of LPTs

The present generation of LPTs typically operates at subsonic conditions, characterised by exit Mach numbers of $Ma_2 \sim 0.6$. The cost of experimental programs can be significantly reduced by performing tests in low-speed wind tunnels, at essentially incompressible conditions. However, the pressure distribution is in general strongly dependent on the Mach number [26]: the peak suction Mach number ultimately controls the adverse pressure

gradient flow region, where most losses are generated. Therefore, experimental testing cannot be carried out on the same blade shape and cascade setup.

A number of scaling techniques as well as more advanced redesign strategies were developed to derive a modified profile shape and flow conditions [27,28], allowing to compensate for the effects of compressibility.

The linear cascade in analysis was redesigned to match the design high Mach number distribution when tested at incompressible conditions, modifying profile shape and increasing the inlet flow angle. This has important implications for the applicability of the capability presented in the paper. One of the main research purposes is the validation of a virtual wind tunnel capability, and the use of an incompressible flow solver is not a road blocker: leveraging scaling techniques, realistic LPT geometries with a peak suction Mach number up to 0.6–0.7 can be accurately simulated in their low-speed testing conditions. However any compressibility effects, even if overall small, are not accounted in the present work.

3. Results

3.1. Evidence of the Transition Mechanism

The time averaging operation masks the wealth of flow phenomena occurring in the boundary layer (BL) of LPTs subject to incoming disturbances, and it particularly fails to highlight the presence of high-amplitude events that precede the onset of turbulence. A discussion on some instantaneous flow statistics is presented before analysing time-averaged statistics, to highlight some of the flow phenomena occurring on the suction surface of the cascade.

Figure 3 provides qualitative insight into the suction surface dynamics at consecutive phases φ for $Re_2 = 86{,}000$. Similar considerations could be discussed for the higher flow regimes $Re_2 = 157{,}000$ and 297,000 but they are here omitted for brevity. The wakes impinge on the suction surface separation bubble between $\varphi = 0.25$ and $\varphi = 0.375$. The extended region of weakly negative recirculation (the pale yellow region) visible at $\varphi = 0$–0.125 between $s/S_0 = 0.7$–0.95 is largely suppressed by the incoming disturbance. Concurrently, at $\varphi = 0.25$ the shear layer rolls up into two separate regions of recirculating flow, as previously highlighted by Michelassi et al. [11]. The upstream recirculation region is found at $s/S_0 \approx 0.85$, while the downstream one merges into the trailing edge. As the wake impacts on the separation bubble, the region of high shear in the upstream portion of the suction surface (the dark blue region) moves towards the trailing edge, following the impinging disturbance. At $\varphi \approx 0.375$, the attached flow region develops a spanwise pattern of alternating high- and low-speed flow, called Klebanoff streaks, which play an important role in the bypass transition mechanism [29,30].

Streaks are found at all the flow regimes analysed, and their spanwise length scale is inversely proportional to the Reynolds number. The generation mechanism of elongated streaks in the suction surface in presence of inflow turbulence was recently discussed in detail by Zhao and Sandberg [31]. In the context of wake passing, the generation of streaks occurs periodically, and its effect on the transition mechanism in the aft portion of the suction surface is evident at $0.375 \leq \varphi \leq 0.75$.

The nature of the disturbances that penetrate the boundary layer shear is determined by the shear sheltering mechanism [32,33]: the boundary layer shear acts as a filter for the high-frequency vortical disturbances. The low-frequency perturbations that penetrate into the boundary layer promote strong shear associated with the streaks, which may develop into turbulent spots through localized secondary streak instability. These steps characterise the early stages of the bypass transition mechanism, described as a secondary instability of lifted shear layers when they reach the top of the boundary layer, and they are subject to high-frequency free-stream disturbances [29,34].

Liu et al. [35] discussed how the physical mechanisms governing streak instability can be revealed through Floquet analysis of secondary instability. As discussed by Zaki [30],

in the presence of Klebanoff streaks the two most unstable modes of the boundary layer are the inner mode (varicose instability) and the outer mode (sinuous instability).

In the early stages of the wake passing cycle, the penetration of streaks within the boundary layer has not reached the trailing edge (TE) region yet. However, the formation of instabilities is detected at $\varphi \approx 0.25$ and highlighted in Figure 4 left; this region is identified by the dashed black rectangle in the third panel of the C_f carpet plots shown on the left. The vorticity contour suggests the presence of part-span K-H instability, which rapidly lifts up from the wall and develops across the boundary layer edge.

The alternating parallel fluctuating velocity patterns are consistent with the findings of Zhao and Sandberg [31], where they are argued to be evidence of varicose streak instability. However, in this case the instability is most likely due to part-span K-H type instability which occurs naturally in the separation bubble. At the later phases of the wake passing cycle, the presence of developed turbulent spots is detected. However, the evidence here presented is not sufficient to uniquely identify the physical streak instability mechanism (i.e., sinuous or varicose) preceding the inception of the spots.

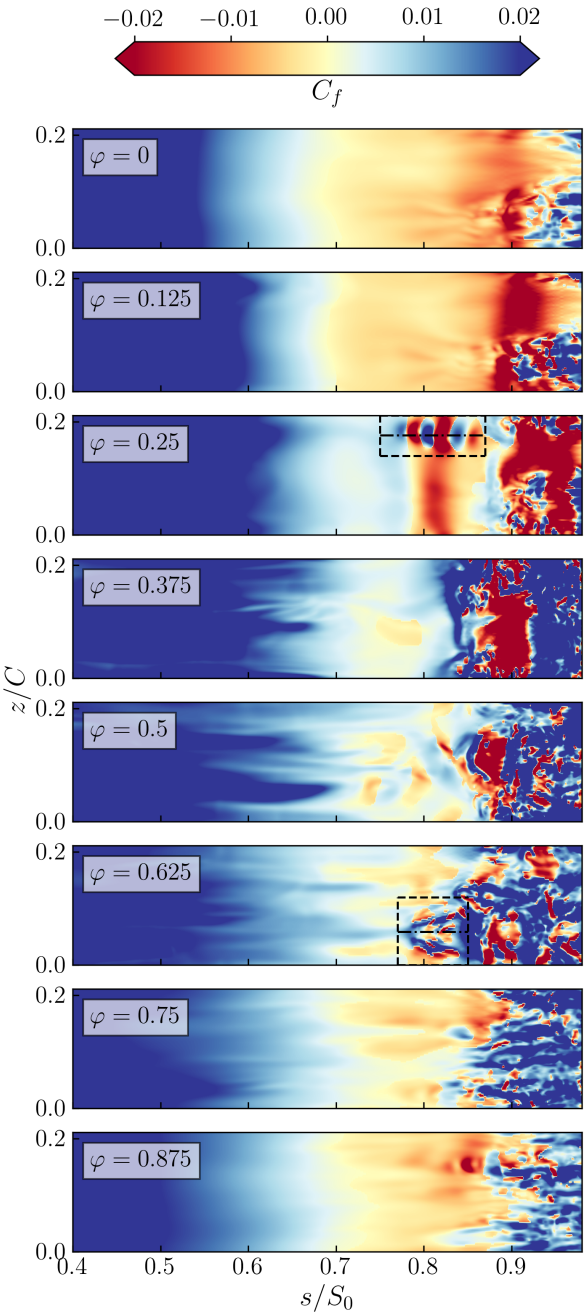


Figure 3. Instantaneous time–space skin friction on the suction surface at eight consecutive phases, $Re_2 = 86{,}000$. The dashed boxes identify the regions shown in detail in Figure 4.

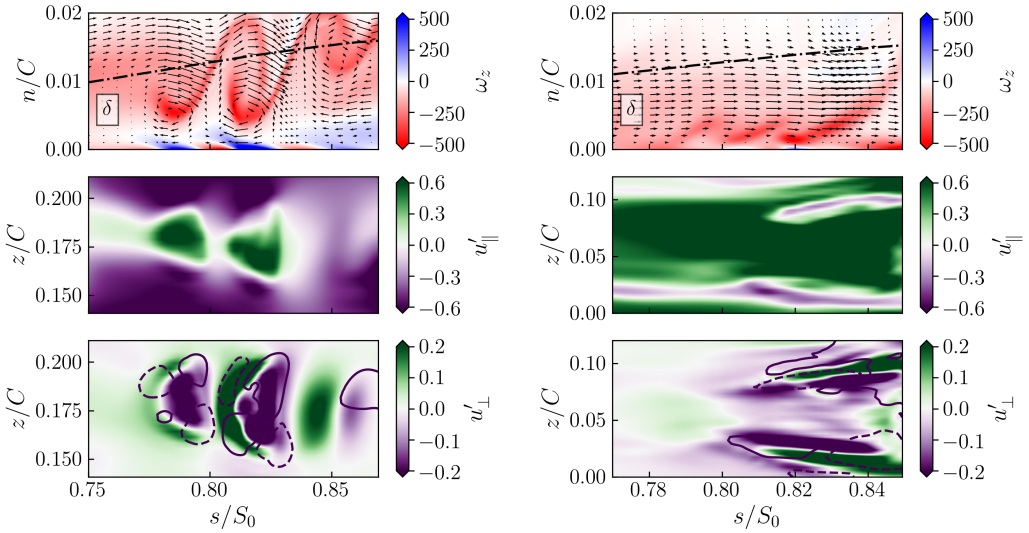


Figure 4. Instantaneous suction surface statistics for $Re_2 = 86{,}000$ in the regions identified by the black dashed boxes of Figure 3. The top subfigure shows spanwise vorticity in the blade-normal plane denoted with dash-dotted lines of Figure 3, superimposed with fluctuating velocity vectors. The middle and bottom figures show respectively wall-parallel and wall-normal fluctuating velocity $n/C = 0.01$ away from the wall. The solid and dashed lines in the bottom subfigures are iso-lines of $w' = \pm 0.15$. (**Left**): $\varphi = 0.25$; (**right**): $\varphi = 0.625$.

3.2. Space-Time Boundary Layer Behaviour

The time evolution of the spanwise-averaged effect of the wakes on the suction surface boundary layer is revealed in the space-time plots of the shape factor of Figure 5. The BL evolution is captured over 4 wake passing periods $\mathcal{T}_b$ with a resolution of 80 flow snapshots per period. Instantaneous statistics are here preferred over phase-averaged realisations to capture the highly unsteady nature of the wake interactions.

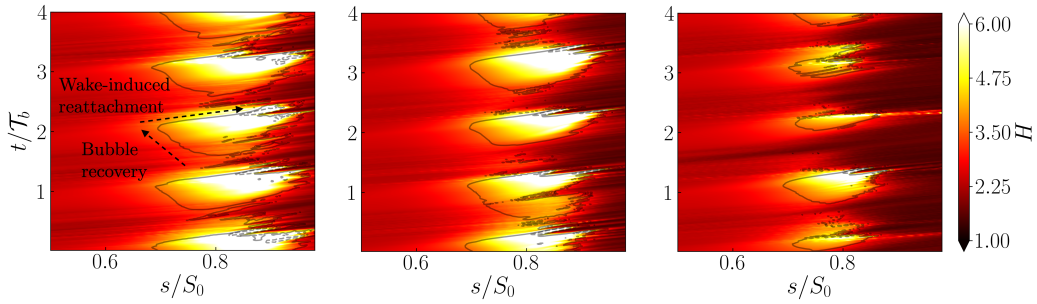


Figure 5. Instantaneous space–time contour of suction surface BL shape factor, superimposed with iso-lines of wall-shear stress at two levels: $C_f = 0$ (continuous line), $C_f = -0.024$ (dashed line). (**Left**): $Re_2 = 86{,}000$; (**middle**): $Re_2 = 157{,}000$; (**right**): $Re_2 = 297{,}000$.

The presence of the separation bubble is highlighted by the solid iso-lines of $C_f = 0$, which identify the spanwise-averaged extent of separation. When the wake interacts with the separation bubble, wake-induced transition promotes reattachment of the flow over the whole extent of the suction surface, as indicated by the dashed arrow on Figure 5. Following the wake-driven reattachment and the subsequent calmed region, the separation bubble recovers as the separation line moves upstream. The separation bubble captured in Figure 5 at $Re_2 = 297{,}000$ is significantly smaller compared to $Re_2 = 86{,}000$; however, it is also subject to larger relative variability in terms of both streamwise and temporal extent: the second instance of separation visualised in Figure 5 is roughly twice as persistent compared to the following instance.

This suggests that the dynamics of the boundary layer between $s/S_0 \approx 0.7 - 0.9$ is largely affected by the presence of streak instabilities trailing the passing of the wake in every cycle.

3.3. Blade Wall Distributions

The time-averaged and spanwise-averaged pressure distribution and skin-friction coefficient are shown in Figure 6. Additional data obtained introducing a momentum forcing near the leading edge (labelled "BF") as described by Cassinelli et al. [13] is included to highlight the impact of the periodic disturbances on time-mean flow performance indicators. Due to the presence of passing bars, the effective inflow angle is decreased compared to the cases without wake passing, from $\alpha_1 = 33.86°$ to $\alpha_1^{\text{eff}} = 31.73°$ in $Re_2 = 86{,}000$, $\alpha_1 = 33.96°$ to $\alpha_1^{\text{eff}} = 32.17°$ in $Re_2 = 157{,}000$ and $\alpha_1 = 34.08°$ to $\alpha_1^{\text{eff}} = 32.18°$ in $Re_2 = 297{,}000$.

The difference translates into discrepancies in the front portion of the suction surface between the cases with and without passing wakes, evident in the suction surface skin friction peak at $s/S_0 \approx 0.05$, where the IW profiles are slightly lower than the cases without incoming wakes. In this same region of the suction surface, lower Reynolds number corresponds to higher wall-shear stress.

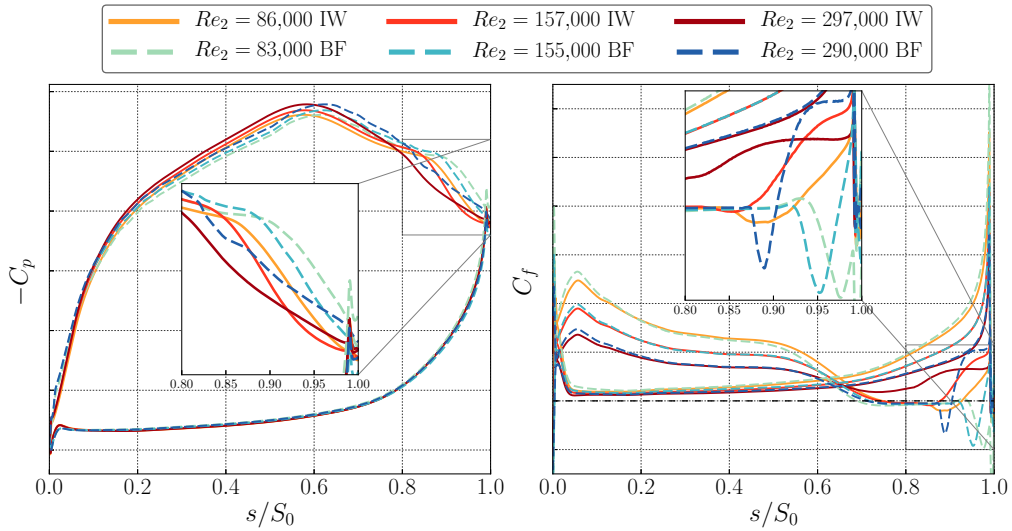


Figure 6. Blade wall distributions with increasing Re_2, compared with momentum forcing cases at the same flow regime. (**Left**): pressure distribution; (**right**): skin-friction coefficient. *Y*-axis tick labels are omitted due to data sensitivity.

The major differences due to the introduction of periodic disturbances are in the adverse pressure gradient part of the suction surface. Especially at low Reynolds numbers, in the C_p distribution the BF cases present a short plateau region at $s/S_0 \approx 0.85$, indicative of a weak separation bubble. This region is delayed and shortened with the introduction of wake passing. The skin-friction coefficient distribution further clarifies the differences. Due to the periodically modified transition mechanism on the suction surface, the wake passing causes an upstream shift of the time-averaged separation bubble at $Re_2 = 86{,}000$ and $Re_2 = 157{,}000$.

In both cases, flow separation occurs at $s/S_0 \approx 0.74$, and the extent of separation is almost halved compared to the cases with body forcing. The negative C_f peak denoting the presence of roll-ups and anticipating reattachment is moved upstream, flattened and only visible at low Reynolds number. This is a consequence of the wake motion along the suction surface and it does not correspond to stationary flow features.

In both cases, $Re_2 = 86{,}000$ and $Re_2 = 157{,}000$, the flow is attached at the trailing edge but not fully developed. Further increasing the Reynolds number ($Re_2 = 297{,}000$)

removes separation in a time-averaged sense and yields a fully turbulent boundary layer at the trailing edge, as highlighted by the flat C_f profile for $s/S_0 > 0.9$.

3.4. Wake Traverses and Experimental Comparison

Extensive experimental data available from LDA measurements are presented in this section. The experimental setup was described in detail by Bolinches-Gisbert et al. [36]. The wake traverses are extracted at $\hat{x} = x - x_{\mathrm{TE}} = 0.513$, and compared with the experiments in Figure 7.

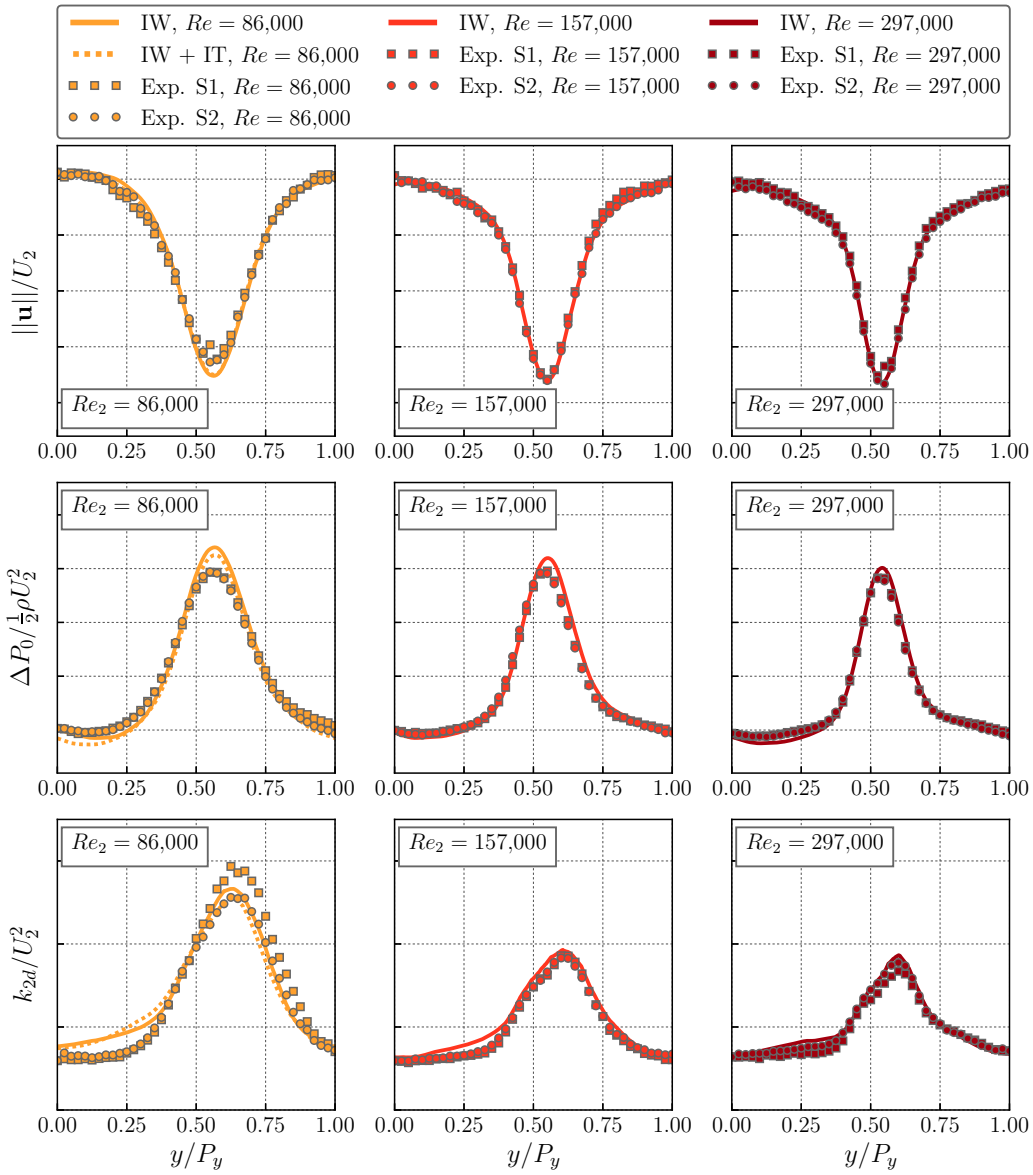


Figure 7. Wake traverses at $\hat{x} = 0.513$ with increasing Reynolds numbers. (**Left**): $Re_2 = 86{,}000$ (in yellow); (**middle**): $Re_2 = 157{,}000$ (in red); (**right**): $Re_2 = 297{,}000$ (in burgundy). Three different wake profiles are shown. (**Top**): velocity magnitude; (**middle**): total pressure loss coefficient; (**bottom**): turbulence kinetic energy. The solid lines indicate IW simulations, and the dashed line indicates IW+IT, for $Re_2 = 86{,}000$ only. The two experimental traverses *S*1 and *S*2 are represented with squares and circles. *Y*-axis tick labels are omitted due to data sensitivity.

The velocity solution accurately captures all the relevant wake flow features, i.e., flank width and negative peak: the latter is within 1% of the experimental value. The presence of

background turbulence (only simulated at $Re = 86{,}000$) does not modify the wake profiles, which overlap to the curves obtained without incoming turbulence, with a marginal discrepancy observed in the mean passage on the pressure side: discrete disturbances are the dominant mechanism in modifying the dynamics of the suction surface separation bubble.

The loss profiles are also reported in the Figure, showcasing good agreement with the experiments especially at higher Reynolds numbers, where the peak is captured within 6% of the experiments. The entity of losses in the mean passage remains unvaried in the three flow regimes explored. The computed results capture a slight decrease of the loss profile peak by ∼6% and 10% in cases $Re_2 = 157{,}000$ and $Re_2 = 297{,}000$, compared to $Re_2 = 86{,}000$.

The experimental values, however, remain approximately constant across the three flow regimes. At higher Re_2, the wake width decreases, owing to the smaller momentum thickness at the trailing edge typical of high-Reynolds configurations, combined with a fully suppressed separation bubble due to bypass transition.

The turbulence length scale in the TE wake was measured from a spanwise line of probe points, yielding a smaller value in the high-Reynolds case, where the two-point correlation decays faster. This in turn promotes lower levels of fluctuations in the wake. At low Re the separation bubble is also periodically open, giving rise to large-scale vortex shedding which results in higher levels of fluctuating turbulence kinetic energy. The higher Reynolds cases $Re_2 = 157{,}000$ and $Re_2 = 297{,}000$ have very similar profiles.

3.5. Mixed-Out Measurements

The mixed-out loss coefficient is shown in Figure 8. The numerical results match the experimental data, with an uncertainty of 2.5% in the total pressure loss coefficient and 0.4 deg of exit angle. At low Reynolds numbers, where the separation periodically extends to the trailing edge, it is traditionally very challenging to accurately capture losses. Case IW + IT at $Re_2 = 86{,}000$ does not improve the agreement with experiments, which were conducted in absence of background fluctuations. The relative error with respect to the experimental measurements is reported in Table 2, which highlights that the two regimes $Re_2 = 86{,}000$ and $Re_2 = 297{,}000$ achieve the minimum error, and are within the range of experimental uncertainty.

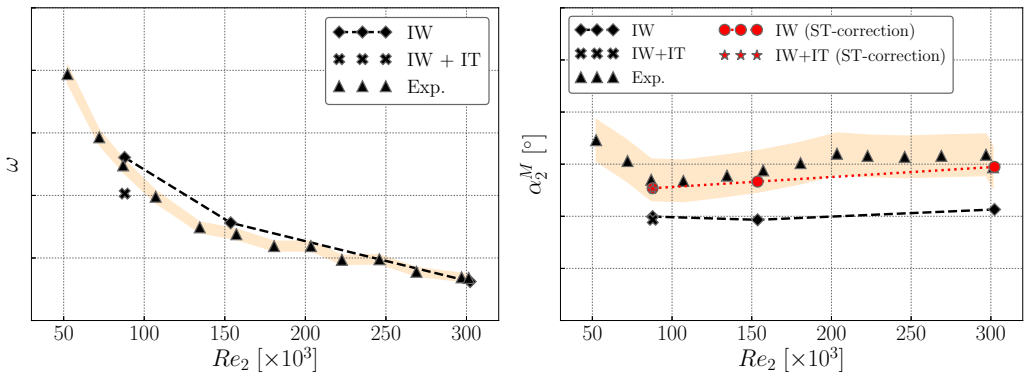


Figure 8. Mixed-out wake traverse measurements: (**left**): total pressure loss coefficient; (**right**): exit angle, with associated streamtube correction shown with red markers. The orange area indicates the uncertainty associated with the measurement chain, of respectively 2.5% and ±0.2°. *Y*-axis tick labels are omitted due to data sensitivity.

The mixed-out exit angle is shown in Figure 8. As highlighted quantitatively in Table 2, the flow turning is consistently overestimated across the flow regimes analysed, suggesting the presence of a bias. The streamwise component of the velocity wakes (not shown) is in deficit compared to the experimental data, especially in the mean passage. Among the various sources of uncertainty between numerical simulations and experiments, the contraction of the experimental streamtube is the most dominant effect. Physically, this

is due to the growth of a boundary layer on the experimental sidewalls, accelerating the flow in the axial direction in the midspan.

A first-order correction is introduced to validate this conjecture, showing that the streamtube effect is mostly responsible for the lack of agreement in the prediction of the exit angle. The ratio between the experimental and computational mass-flow rate k_s can be estimated as:

$$k_s = \frac{\int_0^{p_y} \overline{\mathbf{u}}_{\mathrm{Exp}} \cdot \hat{\mathbf{n}} \, \mathrm{d}y}{\int_0^{p_y} \overline{\mathbf{u}}_{\mathrm{IW}} \cdot \hat{\mathbf{n}} \, \mathrm{d}y} = \frac{\frac{1}{2}(\int_0^{p_y} \overline{u}^{\mathrm{S1}}_{\mathrm{Exp}} \, \mathrm{d}y + \int_0^{p_y} \overline{u}^{\mathrm{S2}}_{\mathrm{Exp}} \, \mathrm{d}y)}{\int_0^{p_y} \overline{u}_{\mathrm{IW}} \, \mathrm{d}y}, \tag{4}$$

considering the average of the mass flow rate calculated in the experimental passages S1 and S2. The streamwise velocity extracted from the numerical simulations is corrected:

$$\overline{u}^{\mathrm{mod}}_{IW} = k_s \overline{u}_{IW}, \tag{5}$$

and the exit angle is recalculated. The associated spanwise domain contraction can be estimated by imposing mass conservation:

$$L'_z = L_z / k_s. \tag{6}$$

The exit angle corrected with the experimental streamtube is consistently shifted to a region within the error bounds of the experimental measurements, therefore suggesting that the streamtube contraction is the physical mechanism responsible for the discrepancy of numerical and experimental measurements. Quantitatively, the mixed-out exit angle error is reduced by ≈80%. The streamtube contraction estimated to yield the correct mass flow rate is between 1–2% and it is larger at higher Reynolds number.

Table 2. Summary of percentage relative error between experimental and computational mixed-out quantity, as well as summary of the streamtube contraction factors.

Parameter	$\boldsymbol{Re_2 = 86{,}000}$	$\boldsymbol{Re_2 = 157{,}000}$	$\boldsymbol{Re_2 = 297{,}000}$
$\frac{\lvert\lvert\omega^M_{\mathrm{IW}} - \omega^M_{\mathrm{Exp}}\rvert\rvert}{\omega^M_{\mathrm{Exp}}}$ [%]	2.919	5.388	2.516
$\frac{\lvert\lvert\alpha^M_{2,\mathrm{IW}} - \alpha^M_{2,\mathrm{Exp}}\rvert\rvert}{\alpha^M_{2,\mathrm{Exp}}}$ [%]	0.563	0.757	0.841
$\frac{\lvert\lvert\alpha^{M,\mathrm{mod}}_{2,\mathrm{IW}} - \alpha^M_{2,\mathrm{Exp}}\rvert\rvert}{\alpha^M_{2,\mathrm{Exp}}}$ [%]	0.129	0.171	0.187
$\frac{L'_z - L_z}{L_z}$ [%]	-1.164	-1.564	-1.734

4. Conclusions

In this paper, we discussed the introduction of the wake-passing effect on an LPT cascade focusing, in particular, on the Reynolds sensitivity of the flow on the suction surface and introducing a comparison of wake measurements with experiments. The three Reynolds numbers analysed correspond to subcritical, critical and supercritical states of the suction surface boundary layer in a clean inflow setup.

The analysis of the LPT flow features first focused on instantaneous statistics. The aft portion of the suction surface features a range of different transition mechanisms, driven by the periodic impingement of the wake passing. At low Reynolds numbers, two roll-up regions were periodically identified where the wake suppresses the suction surface separation bubble; however, at higher Reynolds numbers, this mechanism was not retained. This highlights the high sensitivity of the suction surface separation to external disturbances in the subcritical flow regime.

The comparison of wake traverses from the numerical simulations demonstrates close agreement with experimental measurements with less than a 1% relative error in the profile peak. The total pressure loss coefficient was also predicted accurately, within 5% of the experimental measurements across the flow regimes in analysis. The low- and

high-Reynolds cases were within experimental measurement uncertainty. A first-order estimation suggested that introducing a model of the streamtube contraction of 1–2% of the spanwise domain would yield the same levels of flow turning as in the experiments.

There is a growing need for high-fidelity simulations to train deep neural networks to develop new insights into flow physics. The DNS capability presented in the paper can be used to develop new turbulence closures [37] and promote a better physical understanding of the mechanisms of loss generation in turbomachinery.

Author Contributions: Conceptualization, A.C., F.M., P.A., R.V.D., S.J.S.; data curation, A.C.; formal analysis, A.C.; funding acquisition, F.M., P.A., R.V.D., S.J.S.; investigation, A.C.; methodology, A.C., S.J.S.; project administration, F.M., S.J.S.; resources, A.C., F.M., P.A., R.V.D., S.J.S.; software, A.C., A.M.G., S.J.S.; supervision, F.M., P.A., R.V.D., S.J.S.; validation, A.C.; visualization, A.C.; writing—original draft, A.C.; writing—review and editing, A.C.; All authors have read and agreed to the published version of the manuscript.

Funding: This research received funding from Rolls-Royce plc. and the Aerospace Technology Institute (ATI)/Innovate UK programme "FANFARE".

Data Availability Statement: Due to the nature of funding and the proprietary set of data used, supporting data cannot be made openly available.

Acknowledgments: A.C. would like to acknowledge Vittorio Michelassi, Giacomo Castiglioni and Yuri Frey for the technical discussions. The Authors would also like to acknowledge HPC support from Imperial College Research Computing Service (DOI: 10.14469/hpc/2232) and Archer under the UK Turbulence Consortium (EP/R029326/1).

Conflicts of Interest: The authors declare no conflict of interest.

Abbreviations

The following abbreviations are used in this manuscript:

BF	Body Forcing
BL	Boundary Layer
CFD	Computational Fluid Dynamics
DNS	Direct Numerical Simulation
IW	Inflow Wakes
IT	Inflow Turbulence
LDA	Laser Doppler Anemometry
LES	Large-Eddy Simulation
LPT	Low Pressure Turbine
RANS	Reynolds-Averaged Navier–Stokes
SVV	Spectral Vanishing Viscosity
TI	Turbulence Intensity
URANS	Unsteady RANS

Nomenclature

α	Flow angle
ω	Total pressure loss coefficient
Φ	Flow coefficient
φ	Wake passing phase
$C, (C_{ax})$	Blade (axial) chord length
C_f	Skin friction coefficient
C_p	Static pressure coefficient
F_{red}	Reduced frequency
H	Boundary layer shape factor

k	Turbulence kinetic energy
L_t	Turbulence length scale
L_z	Spanwise domain size
n	Blade wall-normal distance
N_z	Number of Fourier planes
p	Pressure
P	Polynomial order
P_b	Bars pitch
P_y	Blade pitch
Re	Reynolds number
S_0	Suction surface perimeter
T, t	Time
$\mathcal{T}_b$	Wake passing period
U_b	Bar speed
U_2	Mixed-out exit velocity
U_∞	Reference inlet speed

References

1. Wu, X.; Jacobs, R.G.; Hunt, J.C.R.; Durbin, P.A. Simulation of boundary layer transition induced by periodically passing wakes. *J. Fluid Mech.* **1999**, *398*, 109–153. https://doi.org/10.1017/S0022112099006205.
2. Wu, X.; Durbin, P.A. Evidence of longitudinal vortices evolved from distorted wakes in a turbine passage. *J. Fluid Mech.* **2001**, *446*, 199–228. https://doi.org/10.1017/S0022112001005717.
3. Michelassi, V.; Wissink, J.G.; Fröhlich, J.; Rodi, W. Large-Eddy Simulation of Flow Around Low-Pressure Turbine Blade with Incoming Wakes. *AIAA J.* **2003**, *41*, 2143–2156. https://doi.org/10.2514/2.6832.
4. Michelassi, V.; Wissink, J.G.; Rodi, W. Direct numerical simulation, large eddy simulation and unsteady Reynolds-averaged Navier–Stokes simulations of periodic unsteady flow in a low-pressure turbine cascade: A comparison. *Proc. Inst. Mech. Eng. Part A J. Power Energy* **2003**, *217*, 403–412. https://doi.org/10.1243/095765003322315469.
5. Wissink, J.G. DNS of separating, low Reynolds number flow in a turbine cascade with incoming wakes. *Int. J. Heat Fluid Flow* **2003**, *24*, 626–635. https://doi.org/10.1016/S0142-727X(03)00056-0.
6. Wissink, J.G.; Rodi, W. Direct numerical simulation of flow and heat transfer in a turbine cascade with incoming wakes. *J. Fluid Mech.* **2006**, *569*, 209–247. https://doi.org/10.1017/S002211200600262X.
7. Hodson, H.P.; Howell, R.J. Bladerow Interactions, Transition, and High-Lift Aerofoils in Low-Pressure Turbines. *Annu. Rev. Fluid Mech.* **2005**, *37*, 71–98. https://doi.org/10.1146/annurev.fluid.37.061903.175511.
8. Michelassi, V.; Chen, L.; Pichler, R.; Sandberg, R.D. Compressible Direct Numerical Simulation of Low-Pressure Turbines—Part II: Effect of Inflow Disturbances. *J. Turbomach.* **2015**, *137*, 071005. https://doi.org/10.1115/1.4029126.
9. Sandberg, R.D.; Michelassi, V.; Pichler, R.; Chen, L.; Johnstone, R. Compressible Direct Numerical Simulation of Low-Pressure Turbines—Part I: Methodology. *J. Turbomach.* **2015**, *137*, 051011. https://doi.org/10.1115/1.4028731.
10. Denton, J.D. The 1993 IGTI Scholar Lecture: Loss Mechanisms in Turbomachines. *J. Turbomach.* **1993**, *115*, 621–656. https://doi.org/10.1115/1.2929299.
11. Michelassi, V.; Chen, L.; Pichler, R.; Sandberg, R.; Bhaskaran, R. High-Fidelity Simulations of Low-Pressure Turbines: Effect of Flow Coefficient and Reduced Frequency on Losses. *J. Turbomach.* **2016**, *138*, 111006. https://doi.org/10.1115/1.4033266.
12. Cassinelli, A.; Montomoli, F.; Adami, P.; Sherwin, S.J. High Fidelity Spectral/hp Element Methods for Turbomachinery. In Proceedings of the ASME Turbo Expo, 2018; pp. GT2018–75733. https://doi.org/10.1115/GT2018-75733.
13. Cassinelli, A.; Xu, H.; Montomoli, F.; Adami, P.; Vazquez Diaz, R.; Sherwin, S.J. On the Effect of Inflow Disturbances on the Flow Past a Linear LPT Vane Using Spectral/hp Element Methods. In Proceedings of the ASME Turbo Expo, 2019; pp. GT2019–91622.
14. Moxey, D.; Cantwell, C.D.; Bao, Y.; Cassinelli, A.; Castiglioni, G.; Chun, S.; Juda, E.; Kazemi, E.; Lackhove, K.; Marcon, J.; et al. Nektar++: Enhancing the capability and application of high-fidelity spectral/hp element methods. *Comput. Phys. Commun.* **2019**, *249*, 107110. https://doi.org/10.1016/j.cpc.2019.107110.
15. Karniadakis, G.E.; Israeli, M.; Orszag, S.A. High-order splitting methods for the incompressible Navier–Stokes equations. *J. Comput. Phys.* **1991**, *97*, 414–443. https://doi.org/10.1016/0021-9991(91)90007-8.
16. Guermond, J.L.; Shen, J. Velocity-Correction Projection Methods for Incompressible Flows. *SIAM J. Numer. Anal.* **2003**, *41*, 112–134. https://doi.org/10.1137/S0036142901395400.
17. Tadmor, E. Convergence of Spectral Methods for Nonlinear Conservation Laws. *SIAM J. Numer. Anal.* **1989**, *26*, 30–44. https://doi.org/10.1137/0726003.
18. Moura, R.C.; Sherwin, S.J.; Peiró, J. Eigensolution analysis of spectral/hp continuous Galerkin approximations to advection-diffusion problems: Insights into spectral vanishing viscosity. *J. Comput. Phys.* **2016**, *307*, 401–422. https://doi.org/10.1016/j.jcp.2015.12.009.
19. Moura, R.C.; Aman, M.; Peiró, J.; Sherwin, S.J. Spatial eigenanalysis of spectral/hp continuous Galerkin schemes and their stabilisation via DG-mimicking spectral vanishing viscosity for high Reynolds number flows. *J. Comput. Phys.* **2020**, *406*, 109112. https://doi.org/10.1016/j.jcp.2019.109112.

20. Mengaldo, G.; De Grazia, D.; Moxey, D.; Vincent, P.E.; Sherwin, S.J. Dealiasing techniques for high-order spectral element methods on regular and irregular grids. *J. Comput. Phys.* **2015**, *299*, 56–81. https://doi.org/10.1016/j.jcp.2015.06.032.
21. Cassinelli, A. A Spectral/Hp Element DNS Study of Flow Past Low-Pressure Turbine Cascades and the Effects of Inflow Conditions. (Forthcoming). Ph.D. Thesis, 2020.
22. Davidson, L. Using isotropic synthetic fluctuations as inlet boundary conditions for unsteady simulations. *Adv. Appl. Fluid Mech.* **2007**, *1*, 1–35.
23. Nakayama, Y.; Yamamoto, R. Simulation method to resolve hydrodynamic interactions in colloidal dispersions. *Phys. Rev. E* **2005**, *71*, 036707. https://doi.org/10.1103/PhysRevE.71.036707.
24. Luo, X.; Maxey, M.R.; Karniadakis, G.E. Smoothed profile method for particulate flows: Error analysis and simulations. *J. Comput. Phys.* **2009**, *228*, 1750–1769. https://doi.org/10.1016/j.jcp.2008.11.006.
25. Wang, Z.; Triantafyllou, M.S.; Constantinides, Y.; Karniadakis, G.E. A spectral-element/Fourier smoothed profile method for large-eddy simulations of complex VIV problems. *Comput. Fluids* **2018**, *172*, 84–96. https://doi.org/10.1016/j.compfluid.2018.06.022.
26. Vázquez Diaz, R.; Torre, D. The Effect of Mach Number on the Loss Generation of LP Turbines. In Proceedings of the ASME Turbo Expo, 2012; pp. GT2012–68555.
27. Vera, M.; Hodson, H.P. Low Speed Vs High Speed Testing of LP Turbine Blade-Wake Interaction. In Proceedings of the Symposium on Measuring Techniques in Transonic and Supersonic Flow in Cascades and Turbomachines, number September 2002; pp. 1–10.
28. Marconcini, M.; Rubechini, F.; Pacciani, R.; Arnone, A.; Bertini, F. Redesign of High-Lift Low Pressure Turbine Airfoils for Low Speed Testing. *J. Turbomach.* **2012**, *134*, 051017. https://doi.org/10.1115/1.4004474.
29. Jacobs, R.G.; Durbin, P.A. Simulations of bypass transition. *J. Fluid Mech.* **2001**, *428*, 185–212. https://doi.org/10.1017/S0022112000002469.
30. Zaki, T.A. From streaks to spots and on to turbulence: Exploring the dynamics of boundary layer transition. *Flow, Turbul. Combust.* **2013**, *91*, 451–473. https://doi.org/10.1007/s10494-013-9502-8.
31. Zhao, Y.; Sandberg, R.D. Bypass transition in boundary layers subject to strong pressure gradient and curvature effects. *J. Fluid Mech.* **2020**, *888*, A4.https://doi.org/10.1017/jfm.2020.39.
32. Hunt, J.C.; Durbin, P.A. Perturbed vortical layers and shear sheltering. *Fluid Dyn. Res.* **1999**, *24*, 375–404. https://doi.org/10.1016/S0169-5983(99)00009-X.
33. Durbin, P.; Wu, X. Transition Beneath Vortical Disturbances. *Annu. Rev. Fluid Mech.* **2007**, *39*, 107–128. https://doi.org/10.1146/annurev.fluid.39.050905.110135.
34. Zaki, T.A.; Durbin, P.A. Continuous mode transition and the effects of pressure gradient. *J. Fluid Mech.* **2006**, *563*, 357–388. https://doi.org/10.1017/S0022112006001340.
35. Liu, Y.; Zaki, T.A.; Durbin, P.A. Floquet analysis of secondary instability of boundary layers distorted by Klebanoff streaks and Tollmien-Schlichting waves. *Phys. Fluids* **2008**, *20*, 124102. https://doi.org/10.1063/1.3040302.
36. Bolinches-Gisbert, M.; Robles, D.C.; Corral, R.; Gisbert, F. Prediction of Reynolds Number Effects on Low-Pressure Turbines Using a High-Order ILES Method. *J. Turbomach.* **2020**, *142*, 031002. https://doi.org/10.1115/1.4045776.
37. Frey Marioni, Y.; de Toledo Ortiz, E.A.; Cassinelli, A.; Montomoli, F.; Adami, P.; Vazquez, R. A Machine Learning Approach to Improve Turbulence Modelling from DNS Data Using Neural Networks. *Int. J. Turbomachinery, Propuls. Power* **2021**, *6*, 17. https://doi.org/10.3390/ijtpp6020017.